Orthogonal Control of Stability and Tunable Dry Adhesion by Tailoring the Shape of Tapered Nanopillar Arrays

Younghyun Cho, Gyuseok Kim, Yigil Cho, Su Yeon Lee, Helen Minsky, Kevin T. Turner, Daniel S. Gianola, and Shu Yang*

Slender high-aspect-ratio (HAR) fibrils commonly appear in natural dry adhesives, exhibiting high compliance for making contact.[1–11] However, they also tend to collapse when the adhesive energy between each other becomes dominant at sub-micrometer scales,[12,13] thus decreasing the effective contact and dry adhesion strength. While natural HAR fibrils can get away this by hierarchical design and redundancy,[14,15] it is important for synthetic dry adhesives to withstand large deformations and repeated contact while achieving high adhesion strength for their implementation in practical applications. So far, it has been challenging to meet these requirements. Our earlier study suggests that tapered pillars with larger diameter at the bottom than the tips offer higher stability against collapse in comparison to cylindrical ones.[13] A significant technological advancement would be orthogonal control of both stability and dry adhesion strength by tailoring the shape of tapered HAR pillars in the sub-micrometer lengthscales (e.g., spatulae in gecko feet are typically 200–300 nm wide),[2] thus, fine-tuning the nanomechanics of the pillars.

Anodized aluminum oxide (AAO) membranes offer an ideal system to modulate the shape of tapered nanopillars. Since the first report of AAO membranes with highly ordered cylindrical pore arrays realized by secondary anodization, also referred as mild anodization,[16,17] there have been significant interests using AAO membranes as the nanotemplates to create nanowires and nanorods because the anodization process is relatively straightforward and controllable. Structural parameters, including interpore distance (D_{int}), pore depth, and pore size, can be fine-tuned by experimental conditions, including acid composition, concentration, temperature, and applied voltage. Pore size can be further enlarged through postpore widening process while maintaining D_{int}. However, mild anodization itself has rather narrow processing windows and limited choice of D_{int} while maintaining the ordered AAO structures.[16–20] For example, to create tapered AAO membranes with large enough D_{int}, close packed colloidal particles were compressed onto a Al

foil to create nanopits with large enough D_{int}, followed by mild anodization and pore etching.[21]

Lee et al. report a hard anodization process, offering a wider range of D_{int} and at a much faster rate.[22,23] Several pore geometries, including funnel shape, parabola-like ones, and hierarchically branched ones, have been demonstrated by combination of hard and mild anodization.[21,24–26] Nevertheless, systematic variation of the tapered pore shape and study of their shape-dependent mechanical behaviors have yet to be demonstrated.

Here, we created novel tapered nanopillar structures of different cross-sectional geometries over an area of ≈4.9 cm² as depicted in **Figure 1** by infiltration and curing of epoxy resin within the corresponding AAO membranes as templates. First, a hexagonal array of concave pattern in an aluminum plate (2.5 cm in diameter) was generated by hard anodization, which was then utilized as a nucleation seed for the mild anodization. Typical D_{int} obtained from mild anodization ranges from 30–60 nm from sulfuric acid, 80–140 nm from oxalic acid, and 450–500 nm from phosphoric acid.[22] However, it has not been possible to realize intermediate D_{int}. In contrast, a hard anodization process provides a much wider self-ordering processing window with D_{int} in the range of 80–370 nm. In order to realize the AAO template with various tapered porous structures and utilize it as a template for the preparation of polymer nanopillars, it is essential to control D_{int} in the larger end of the range (200–400 nm). If D_{int} is too small compared to the pore diameter, there will be little room for further pore enlargement. Conversely, if D_{int} is too large, the pore density and pillar density decrease, thus lowering adhesion force of nanopillars due to decreased contact area. D_{int} can be fine-tuned from 260 to 350 nm by applying a voltage at 120–160 V during hard anodization. In our study, the applied voltage for hard anodization was fixed at 160 V to obtain $D_{int} \approx 350$ nm, allowing for sufficient room for additional pore widening to realize various cross-sections. The vertical pore growth was controlled by anodization time at a rate of 0.5–0.6 nm s⁻¹, while the pore diameter was enlarged by the additional pore etching process, which determines the lateral pore growth (Figure S1, Supporting Information). Here, we fabricated tapered structures with precisely tailored size and shape, including tall and short cone-shaped, pencil-like, and stepwise nanopillars, by fine-tuning anodization time (t_A), pore etching time (t_{PE}), and the number of reaction cycles (n). After filling up AAO templates with epoxy resin, followed by curing, the AAO template and the bottom aluminum layer were removed by wet-chemical etching to obtain the epoxy nanopillar arrays.

Figure 2 shows field-emission scanning electron microscopy (FE-SEM) images of various tapered AAO templates

Dr. Y. Cho, Dr. G. Kim, Dr. Y. Cho, Dr. S. Y. Lee,
Prof. D. S. Gianola, Prof. S. Yang
Department of Materials Science and Engineering
University of Pennsylvania
3231 Walnut Street, Philadelphia, PA 19104, USA
E-mail: shuyang@seas.upenn.edu
H. Minsky, Prof. K. T. Turner
Department of Mechanical Engineering and Applied Mechanics
University of Pennsylvania
220 South 33rd Street, Philadelphia, PA 19104, USA
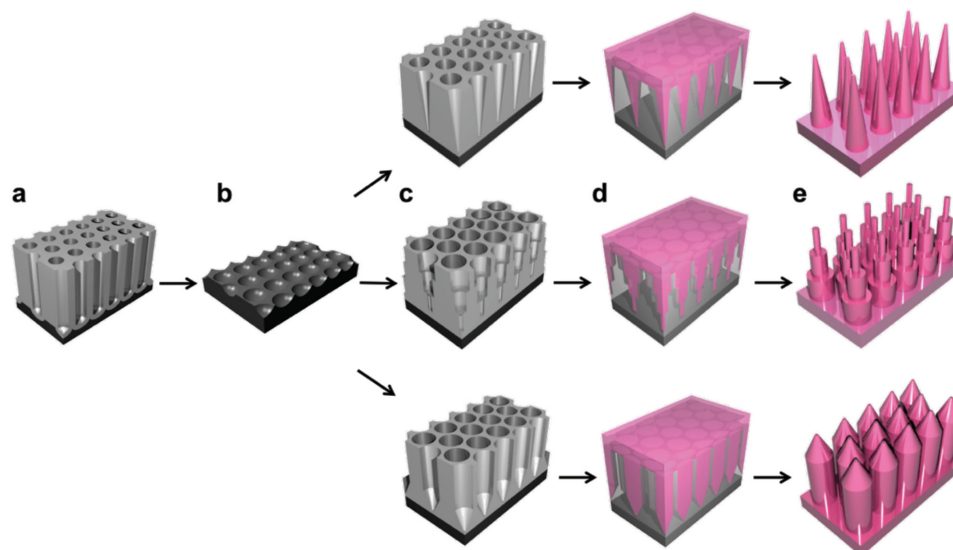
COMMUNICATION

Figure 1. Schematics of the process flow for the preparation of tapered nanopillar arrays; a) synthesis of the AAO membrane by hard anodization, b) removal of the alumina layer, c) combination of mild anodization and pore etching at various conditions, d) infiltration of epoxy resin, followed by UV curing, and e) removal of the AAO template.

(Figure 2a–d) and the corresponding epoxy nanopillars replicated from AAO templates (Figure 2e–h). The D_{int} of AAO prepared by conventional mild anodization has a linear dependence on the applied voltage at 2.5 nm V^{-1}. For hard anodization, D_{int} = 350 nm at an applied voltage of 160 V, we opted for mild anodization at a voltage of 140 V. Anodization time (t_A) and pore etching time (t_{PE}) were determined by the vertical depth and the lateral pore size of a designed tapered AAO template (see details in the Supporting Information). Overall, the tapered pores had depth of 1.1 µm and the maximum pore diameter was 300 nm. Although higher aspect ratio (>10) nanopillars could also be obtained by our method, they tend to collapse under load, making it difficult to study shape-dependent dry adhesion at the contact interface.

One distinct advantage of the tapered nanopillars is their high stability compared to the cylindrical nanopillars when

dried from the acidic solution for removal of the AAO template. Nanopillars can easily aggregate, forming a cluster when the elastic restoring force of the pillars cannot overcome the capillary force upon drying. The bending moment (τ_c) on the single nanopillar originated form capillary force between two neighboring cylinders can be expressed as:

$$\tau_c = \frac{\pi \gamma d^2 h \cos^2 \theta}{2\sqrt{p^2 - d^2}} \qquad (1)$$

where γ is the surface tension of liquid, d and h are the diameter and height of a nanopillar, respectively. θ is the contact angle of the liquid on the nanopillars and p is the center-to-center distance between the nanopillars, equivalent to D_{int} here.[27–29] In tapered structures, as the diameter of nanopillars decreases from the bottom to top, the bending moment
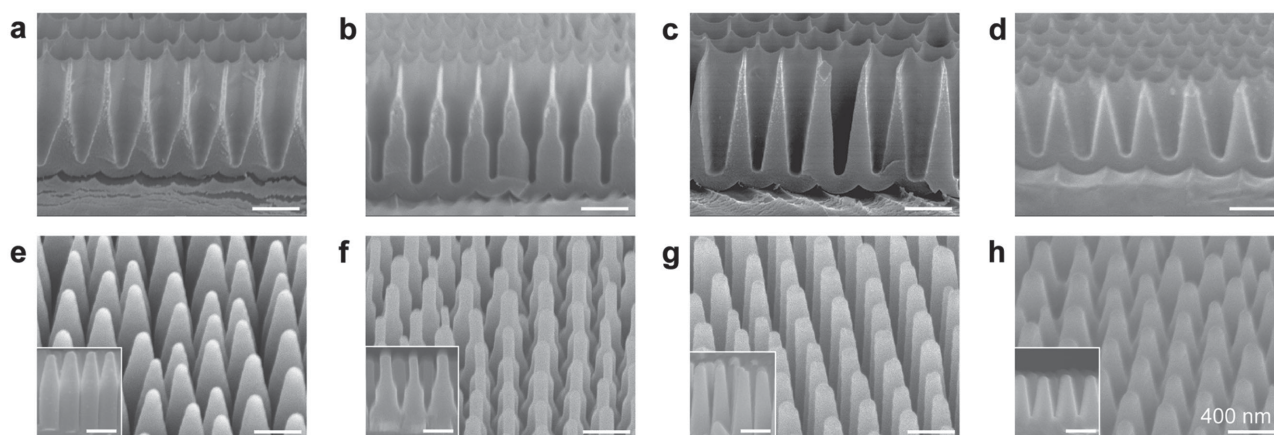

Figure 2. FE-SEM images of: a–d) various tapered AAO templates and e–h) their replica to epoxy nanopillar arrays; a) pencil-like, b) stepwise, c) tall cone-shaped, and d) short cone-shaped. e–h) The corresponding epoxy nanopillar arrays templated from the AAO membranes shown in (a)–(d). The insets of (e)–(h) show the cross-sectional view of each epoxy structure. Scale bars in all panels and the insets: 400 nm.
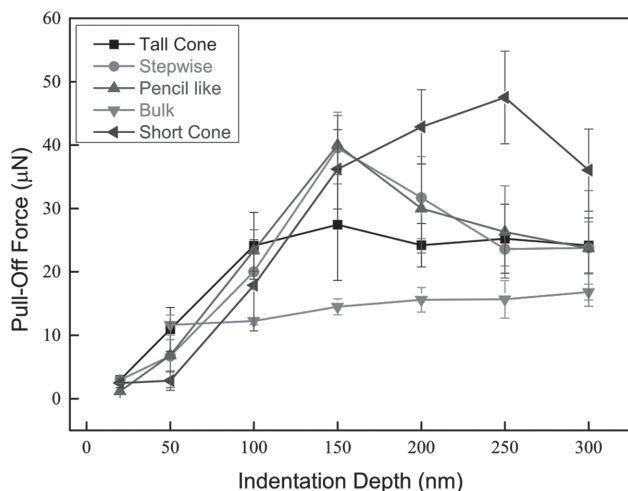
Figure 3. Pull-off force between the tapered epoxy nanopillar arrays and the nanoindenter as a function of the indentation depth using a cono-spherical diamond tip with a nominal radius of 100 μm.

drastically decreases due to the larger interpillar spacing at pillar tops, allowing for highly stable nanopillar arrays without clustering or bending even after the liquid dries, which is in sharp contrast to the observed clustering of cylindrical nanopillars with a similar aspect ratio (see Figure S2, Supporting Information).

Having stable nanopillars at our disposal, we then performed nanoindentation experiments and the adhesion force of nanopillar arrays was measured from the pull-off force between the tapered epoxy nanopillars and the indentation tip. As shown in **Figure 3**, the pull-off force between the tapered epoxy nanopillars and the indentation tip showed quite different trends from different shaped pillars as the indentation depth increased to 300 nm. Overall, they all exhibited much higher adhesion force than the bulk epoxy, which only slightly increased (up to 14 μN). It is expected that the bulk sample should have the largest contact area when both the probe and sample are perfectly smooth. However, as shown in Figure S3 (Supporting Information), it is difficulty to prepare a perfectly smooth surface; the root-mean square roughness of our bulk sample is 3.02 nm measured from atomic force microscopy. Therefore, we anticipate that the effective contact area between the nanostructured surface and indenter tip is larger than that of a randomly rough bulk film and the stress concentration on nanostructure can be more uniformly distributed in nanopillars due to equal load sharing,[4] resulting in a larger adhesion force for all the tapered nanopillars except the nondeformed state. As the indentation depth increases, the effective contact area between the epoxy surface and indenter tip increases. In the case of tall cone-shaped nanopillars, the pull-off force gradually increased with indentation depth (up to 28 μN) and remained above 22 μN without further reduction at a higher indentation depth. Similarly, the adhesion force of short cone-shaped nanopillars increased continuously up to 48 μN as the indentation depth increased but began to drop at the indentation depth of 300 nm. Importantly, the adhesion force is three times higher than that of the bulk at the indentation depth of 250 nm. In comparison, a transition at the indentation depth of

150 nm for stepwise and pencil-like nanopillars was observed, where the force reached a maximum, ≈40 μN, close to that of short cone-shaped nanopillars but dropped sharply to ≈24 μN at the indentation depth of 300 nm. The sudden drop of adhesion force in these pillar systems seems to suggest unrecoverable mechanical deformation in pillars beyond 150 nm, which coincides with the height of the first step in stepwise pillars. Furthermore, the adhesion behaviors at the different preload were investigated (see Figure S4, Supporting Information). For a given indentation depth, the preload applied to the nanopillars varied depending on the shape of nanopillars (Figure S4a, Supporting Information). As we discuss in more details below, this could be attributed to the shape-dependent mechanical responses under the load, leading to different pull-off force (Figure S4b, Supporting Information).

To better understand the effect of contact area during indentation and thus shape effect on nanopillar dry adhesion strength, we instrumented in situ flat punch indentation in FE-SEM according to the literature[30] to directly visualize the pillars during loading and unloading. As seen in **Figure 4**, it is clear that the contact between the indenter and the nanopillar surface, and nanopillars' deformation and recovery behaviors are quite different for different shaped pillars.

The bending stiffness is determined by the elastic materials properties and pillar geometry, including the Young's modulus and dimensions of nanopillars (e.g., diameter and height).[31–33] When the indentation force exceeds the critical fracture load of the nanopillars, mechanical failure occurs. Multiple fracture sites were observed in pencil-like and stepwise shaped nanopillars after indentation, whereas no fracture was generated for the cone-shaped nanopillars under the same applied displacement. Specifically, cracks were first generated mainly in the upper part of the pencil-like nanopillars, followed by fracture in the middle region consisting of cylindrical nanopillars. In the case of stepwise nanopillars, fracture was generated mainly at the transition region between the top and middle structures at the beginning of indentation (see Figure 4b and Figure S5, Supporting Information), which is ≈150 nm depth. As the indentation depth increased, fracture began to appear at the region between the middle and bottom structures (Figure S6, Supporting Information). These observations qualitatively agree with the pull-off force trend shown in ex situ nanoindentation measurement. In the case of short and tall cone-shaped nanopillars, they were continuously bent instead of fracture under the load till reaching the maximum indentation depth (≈400 nm). Upon unloading, the deformed pillars recovered as shown in the Video S1–S4 (Supporting Information). Since dry adhesion force is mainly determined by the van der Waals interactions between two surfaces, the effective contact is critically important. For pencil-like and stepwise shaped nanopillars, since they are already destroyed when the indentation depth exceeds a certain point (150 nm in Figure 3), they cannot be fully recovered and maintain conformal contact during the loading and unloading processes, resulting in a significant drop in adhesion force. In contrast, for short and tall cone-shaped nanopillars, they can endure the external stress even at higher indentation depths without any fracture generation or other inelastic deformation. Therefore, they can keep conformal contact with the indentation tip via bending and be recovered
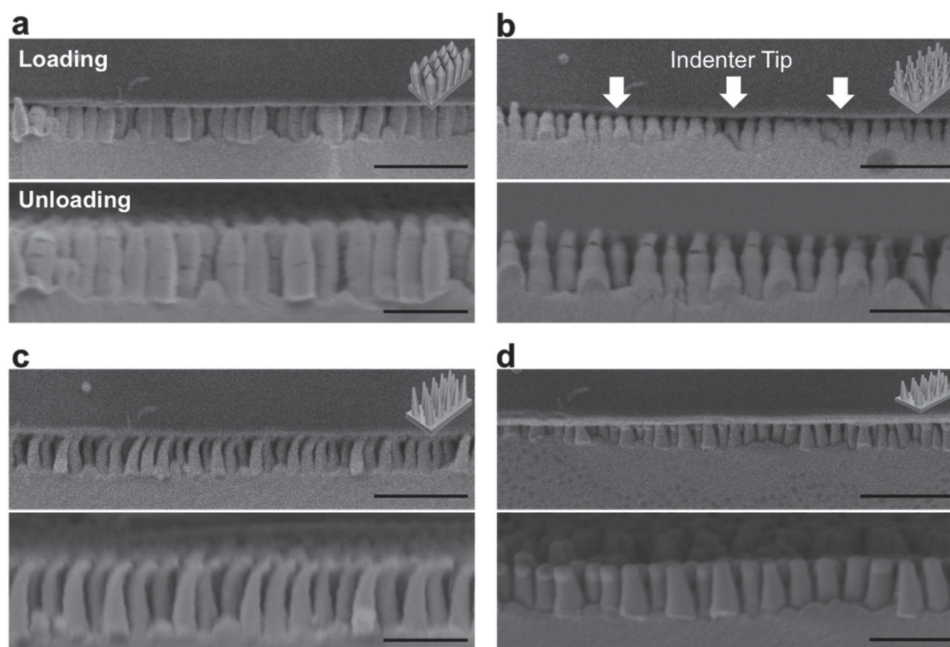
Figure 4. In situ FE-SEM images of various epoxy nanopillars during the loading (top panel) and unloading (bottom panel) of the nanoindenter at the indentation depth of 400 nm. a) Pencil-like, b) stepwise, c) tall cone-shaped, and d) short cone-shaped epoxy nanopillar arrays. The top images represent the nanopillars at the maximum indentation depth (400 nm); the bottom images represent the nanopillars after unloading. Scale bars in the top and bottom images of each panel are 2 μm and 1 μm, respectively.

when the stress reduces, preventing the loss in adhesion force at higher indentation depth.

To quantitatively understand the origin of the observed in situ behavior and thus the shape effect on mechanical responses of various tapered nanopillars, we simulated the pillar deformation modes using finite element analysis. Here, static analyses were performed since the strain rate for in situ SEM indentation experiments was fixed as 0.0025 s^{-1}. Likewise, time-dependent material properties, i.e., viscoelasticity and plasticity, were not considered here. Sixteen pillars (4 × 4 array, ≈1–2 μm × 1–2 μm area) beneath the spherical indenter tip (nominal radius of 100 μm) were considered in each simulation. We note that while we observed randomly bent pillars in simulation when the tip contact was located at the center of the pillar array, in in situ FE-SEM we often observed pillars bent in the same direction, which could be attributed to specimen alignment during indentation and the small imaging regions. Therefore, we adjusted the tip position in simulation to the edge of the pillar array to better correlate the experimental observations, at least at the local regions. As seen in **Figure 5**, at the beginning of indentation, the von Mises stress is concentrated on the tip of each pillar. For pencil-like nanopillars, as the indentation depth increases, stress is first focused in the middle of upper cone part of each nanopillar. Therefore, first fractures are normally generated at this point. The deformation further develops as the stress is spread out toward the cylindrical part of nanopillars (indentation depth > 150 nm), resulting in second fracture at the cylindrical part. The observations of stress localization in different shaped nanopillars from simulation agree well with that from in situ FE-SEM images (Figure 4a and Figure S5, Supporting Information). Likewise for stepwise

nanopillars, the stress is mainly localized at the joint regions where the cylinders of different diameters meet (see Figure 5b). The stress concentration in the joint regions is over 1 GPa at the indentation depth of 400 nm, while the stress develops less than 500 MPa for rest of the regions. Therefore fractures occur only at specific locations, i.e., the transition regions between the first and second cylinders and the second and third cylinders in the stepwise shaped nanopillars, where the sharp changes in these regions locally raise the stress dramatically (see Figure 4b and Figure S6 and Video S1 and S2, Supporting Information). For short and tall cone-shaped nanopillars with continuous geometrical change at the sidewalls of the pillars, the stress distribution of each nanopillar is relatively uniform compared to the pencil-like and stepwise nanopillars, which have the discontinuity in geometry along the pillar height. This indicates that the cone-shaped nanopillars can effectively accommodate the external stress, preventing the fracture formation as observed in pencil-like and stepwise nanopillars. It is worth noting that at the same indentation depth the short cone-shaped nanopillars undergo larger deformation than the other three shapes due to its shorter initial height. However, the higher stress level of the short cone-shaped nanopillars than that from the other three shapes does not necessarily indicate the higher stress concentration (see Figure S7, Supporting Information). Therefore, the cone-shaped nanopillars can maintain conformal contact with the indentation tip where the adhesion force gradually increases with indentation depth, whereas the fracture formation seriously reduces the adhesion force of the pencil-like and stepwise nanopillars. Furthermore, the simulation result shows that the effective contact area of various epoxy nanopillars varies depending on their different geometries (Figure S8, Supporting
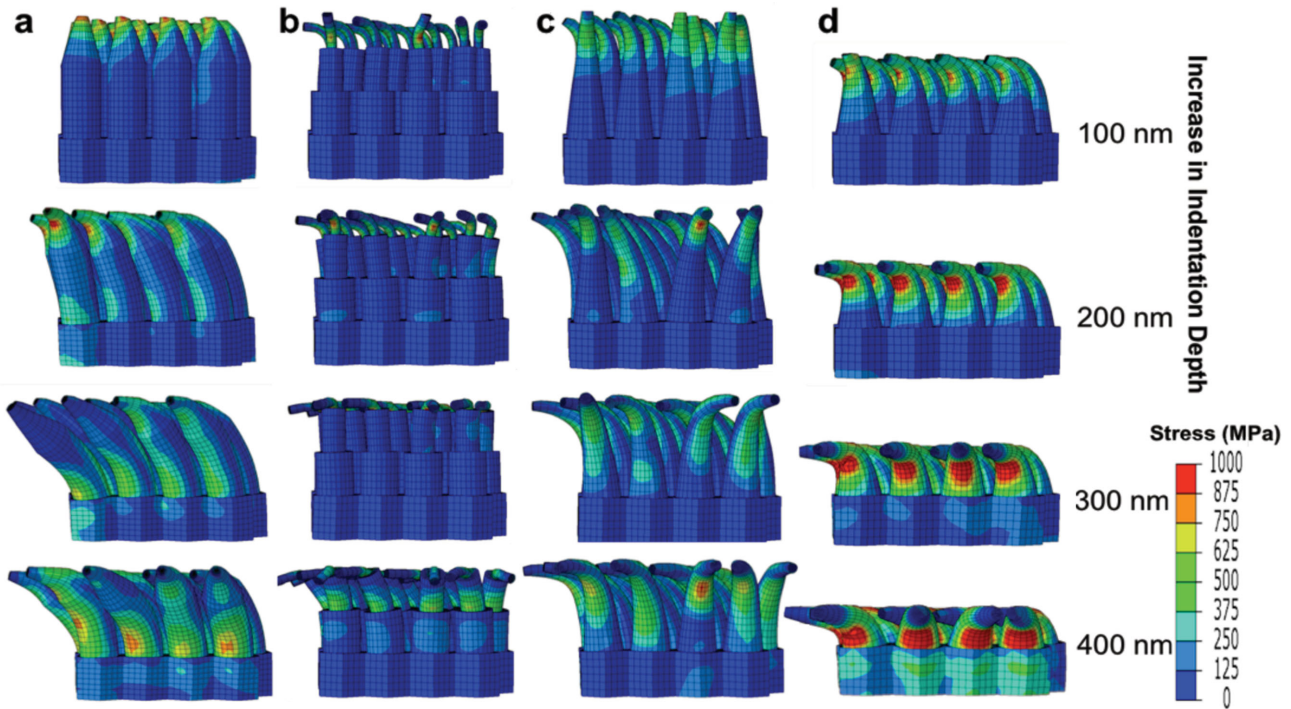
Figure 5. Finite element simulation of the contact process between various tapered epoxy nanostructures and nanoindenter tip as a function of indentation depth. a) Pencil-like, b) stepwise, c) tall cone-shaped, and d) short cone-shaped structures. (Contour: von Mises stress.)

Information). Among them, the contact area of short cone-shaped nanopillar gradually increases with higher indentation depth, leading to the highest adhesion strength. In comparison, the fracture formation in pencil-like and stepwise shaped structures significantly reduces the contact area, and thus dry adhesion strength. After normalizing the pull-off force in Figure 3 by the projected contact area between the indentation tip and nanopillars before fracture, we found that pencil-like and stepwise nanopillars had the highest dry adhesion strength, i.e., 42 N cm^{-2} in the normal direction for the indentation depth of 150 nm (see Figure S9, Supporting Information). At indentation depth larger than 150 nm, due to fracture formation, the effective contact area changed. Thus, the calculated value does not represent the true adhesion strength. In comparison, recoverable short cone-shaped structures showed the highest value of 34 N cm^{-2} without fracture formation at 200 nm indentation depth. These values are among the highest reported dry adhesion strength of pillar-to-flat surfaces in the normal direction regardless of fracture generation, which typically ranges from 10 to 20 N cm^{-2}.[34–37]

In summary, we prepared a new type of tapered epoxy nanopillar arrays from AAO templates with various cross-sections, including cone-shaped (tall and short), pencil-like, and stepwise, through the combination of hard and mild anodization, followed by pore etching and replica molding. Compared to cylindrical pillars, these tapered pillars are highly stable against capillary force. We then investigated shape effect to dry adhesion strength by performing nanoindentation experiments both ex situ and in situ in SEM in comparison with finite element analysis. The pencil-like and stepwise nanopillars showed the highest dry adhesion strength of 42 N cm^{-2} in the normal

direction among different pillars without fracturing, which is the highest reported value for synthetic gecko-like adhesives. The adhesion strength of short cone-shaped nanopillars remained high, 34 N cm^{-2}, when pencil-like and stepwise nanopillars began to fracture at a higher indentation depth, where the adhesive strength dropped significantly. This could be explained by the more uniform stress distribution throughout the short cone-shaped nanopillars, thus preventing fracture formation observed in other nanopillar structures. Importantly, upon removal of the load, the deformed short cone-shaped pillars are mostly recovered. While higher dry adhesion strength has been reported based on the interlocking mechanisms from micropillar-to-micropillar,[36] which typically have a much higher adhesion strength than gecko-like pillar-to-flat surface, the resulting adhesive is irreversible. Since the cone-shaped nanopillars are not 100% recoverable, some deformation still occurs, we expect the adhesion strength will gradually decrease in repeated indentations. Nevertheless, the investigation of shape effect on mechanical response of nanopillars under load presented here offers new insights to design the geometry of nanostructures to achieve high mechanical stability and high and tunable adhesion strength orthogonally, which so far has not been possible in synthetic pillar structures reported in the literature. Yet to implement synthetic dry adhesives for repeated usages, both high mechanical robustness and tunable adhesion strength are critical. Furthermore, our fabrication of nanostructures using AAO template can be scaled-up simply by using a larger aluminum plate. Although we focused study on shape-dependent dry adhesion strength here, tapered structures are of interests for a variety of potential applications, including water harvesting, reducing light reflection at the interface, broadband

COMMUNICATION

absorption, light guidance, and many other unique surface properties.

Supporting Information

Supporting Information is available from the Wiley Online Library or from the author.

Acknowledgements

[1] E. Lee, S. Yang, *MRS Commun.* **2015**, *1*, 1.
[2] K. Autumn, Y. A. Liang, S. T. Hsieh, W. Zesch, W. P. Chan, T. W. Kenny, R. Fearing, R. J. Full, *Nature* **2000**, *405*, 681.
[3] L. J. Xue, A. Kovalev, F. Thole, G. T. Rengarajan, M. Steinhart, S. N. Gorb, *Langmuir* **2012**, *28*, 10781.
[4] C. Y. Hui, N. J. Glassmaker, T. Tang, A. Jagota, *J. R. Soc. Interface* **2004**, *1*, 35.
[5] A. del Campo, C. Greiner, E. Arzt, *Langmuir* **2007**, *23*, 10235.
[6] M. P. Murphy, S. Kim, M. Sitti, *ACS Appl. Mater. Interfaces* **2009**, *1*, 849.
[7] S. Kim, E. Cheung, M. Sitti, *Langmuir* **2009**, *25*, 7196.
[8] A. K. Geim, S. V. Dubonos, I. V. Grigorieva, K. S. Novoselov, A. A. Zhukov, S. Y. Shapoval, *Nat. Mater.* **2003**, *2*, 461.
[9] C. S. Majidi, R. E. Groff, R. S. Fearing, *J. Appl. Phys.* **2005**, *98*, 103521.
[10] N. J. Glassmaker, A. Jagota, C. Y. Hui, W. L. Noderer, M. K. Chaudhury, *Proc. Natl. Acad. Sci. USA* **2007**, *104*, 10786.
[11] H. E. Jeong, J. K. Lee, M. K. Kwak, S. H. Moon, K. Y. Suh, *Appl. Phys. Lett.* **2010**, *96*, 043704.
[12] N. J. Glassmaker, A. Jagota, C. Y. Hui, J. Kim, *J. R. Soc. Interface* **2004**, *1*, 23.
[13] Y. Zhang, C. W. Lo, J. A. Taylor, S. Yang, *Langmuir* **2006**, *22*, 8595.
[14] W.-G. Bae, H. N. Kim, D. Kim, S.-H. Park, H. E. Jeong, K.-Y. Suh, *Adv. Mater.* **2014**, *26*, 675.
[15] H. E. Jeong, J. K. Lee, H. N. Kim, S. H. Moon, K. Y. Suh, *Proc. Natl. Acad. Sci. USA* **2009**, *106*, 5639.
[16] H. Masuda, K. Fukuda, *Science* **1995**, *268*, 1466.
[17] H. Masuda, F. Hasegwa, S. Ono, *J. Electrochem. Soc.* **1997**, *144*, L127.
[18] A. P. Li, F. Muller, A. Birner, K. Nielsch, U. Gosele, *J. Appl. Phys.* **1998**, *84*, 6023.
[19] F. Y. Li, L. Zhang, R. M. Metzger, *Chem. Mater.* **1998**, *10*, 2470.
[20] K. Nielsch, J. Choi, K. Schwirn, R. B. Wehrspohn, U. Gosele, *Nano Lett.* **2002**, *2*, 677.
[21] C. S. Li, J. Li, C. Chen, J. Zhu, X. F. Gao, *Chem. Commun.* **2012**, *48*, 5100.
[22] W. Lee, R. Ji, U. Gosele, K. Nielsch, *Nat. Mater.* **2006**, *5*, 741.
[23] K. Schwirn, W. Lee, R. Hillebrand, M. Steinhart, K. Nielsch, U. Gosele, *ACS Nano* **2008**, *2*, 302.
[24] G. Meng, Y. J. Jung, A. Cao, R. Vajtai, P. M. Ajayan, *Proc. Natl. Acad. Sci. USA* **2005**, *102*, 7074.
[25] M. Kim, Y. C. Ha, T. N. Nguyen, H. Y. Choi, D. Kim, *Nanotechnology* **2013**, *24*, 505304.
[26] J. Liu, S. Liu, H. H. Zhou, C. J. Xie, Z. Y. Huang, C. P. Fu, Y. F. Kuang, *Thin Solid Films* **2014**, *552*, 75.
[27] D. Chandra, S. Yang, *Langmuir* **2009**, *25*, 10430.
[28] D. Chandra, S. Yang, *Acc. Chem. Res.* **2010**, *43*, 1080.
[29] H. Yoon, M. K. Kwak, S. M. Kim, S. H. Sung, J. Lim, H. S. Suh, K. Y. Suh, K. Char, *Small* **2011**, *7*, 3005.
[30] X. Y. Zhao, D. J. Strickland, P. M. Derlet, M. R. He, Y. J. Cheng, J. Pu, K. Hattar, D. S. Gianola, *Acta Mater.* **2015**, *88*, 121.
[31] H. J. Qi, K. B. K. Teo, K. K. S. Lau, M. C. Boyce, W. I. Milne, J. Robertson, K. K. Gleason, *J. Mech. Phys. Solids* **2003**, *51*, 2213.
[32] L. F. Wang, C. Ortiz, M. C. Boyce, *ASME J. Eng. Mater. Technol.* **2011**, *133*, 011014.
[33] E. W. Wong, P. E. Sheehan, C. M. Lieber, *Science* **1997**, *277*, 1971.
[34] B. G. Chen, G. F. Zhong, P. G. Oppenheimer, C. Zhang, H. Tornatzky, S. Esconjauregui, S. Hofmann, J. Robertson, *ACS Appl. Mater. Interfaces* **2015**, *7*, 3626.
[35] L. T. Qu, L. M. Dai, M. Stone, Z. H. Xia, Z. L. Wang, *Science* **2008**, *322*, 238.
[36] C. M. Chen, C. L. Chiang, C. L. Lai, T. Xie, S. Yang, *Adv. Funct. Mater.* **2013**, *23*, 3813.
[37] Y. Zhao, T. Tong, L. Delzeit, A. Kashani, M. Meyyappan, A. Majumdar, *J. Vac. Sci. Technol. B* **2006**, *24*, 331.